Unravelling Kinetic and Thermodynamic Effects on the Growth of Gold Nanoplates by Liquid Transmission Electron Microscopy

Damien Alloyeau, Walid Dachraoui, Yasir Javed, Hannen Belkahla, Guillaume Wang, Hélène Lecoq, Souad Ammar, Ovidiu Ersen, Andreas Wisnet, Florence Gazeau, et al.

Unravelling Kinetic and Thermodynamic Effects on the Growth of Gold Nanoplates by Liquid Transmission Electron Microscopy

Damien Alloyeau,[1] Walid Dachraoui,[1] Yasir Javed,[1] Hannen Belkahla,[2] Guillaume Wang,[1] Hélène Lecoq[2], Souad Ammar,[2] Ovidiu Ersen,[4] Andreas Wisnet,[5] Florence Gazeau,[3] Christian Ricolleau.[1]*

[1] Laboratoire Matériaux et Phénomènes Quantiques, UMR 7162 CNRS/Université Paris - Diderot, 10 rue Alice Domon et Léonie Duquet, 75013 Paris, France.

[2] Interfaces Traitements Organisation et Dynamique des Systèmes, UMR7086 CNRS/Université Paris - Diderot, 15, rue Jean-Antoine de Baïf, 75013 Paris, France.

[3] Laboratoire Matières et Systèmes Complexes, UMR 7057 CNRS/Université Paris - Diderot, 10 rue Alice Domon et Léonie Duquet, 75013 Paris, France.

[4] Institut de Physique et Chimie des Matériaux de Strasbourg (IPCMS, UMR 7504 CNRS-UDS), 23 rue du Loess BP 43 F-67034, Strasbourg Cedex 2, France.

[5] Department of Chemistry and CeNS, Ludwig-Maximilians-University, Butenandtstr. 11, 81377 Munich, Germany.

ABSTRACT

The growth of colloidal nanoparticles is simultaneously driven by kinetic and thermodynamic effects that are difficult to distinguish. We have exploited *in situ* scanning transmission electron microscopy in liquid to study the growth of Au nanoplates by radiolysis and unravel the mechanisms influencing their formation and shape. The electron dose provides a straightforward control of the growth rate which allows quantifying the kinetic effects on the planar nanoparticles formation. Indeed, we demonstrate that the surface-reaction rate per unit area has the same dose-rate dependent behavior than the concentration of reducing agents in the liquid cell. Interestingly, we also determine a critical supply rate of gold monomers for nanoparticle faceting, corresponding to three layers per second, above which the formation of nanoplates is not possible because the growth is then dominated by kinetic effects. At lower electron dose, the growth is driven by thermodynamic and the formation and shape of nanoplates are directly related to the twin-planes formed during the growth.

KEYWORDS: Gold nanoplates, *in situ* liquid transmission electron microscopy, dose rate, growth, kinetic effects, twinning.

Understanding the growth mechanisms of nanomaterials is an essential prerequisite for controlling their shape-dependant properties. In that regard, metallic nanoplates have attracted the attention of colloidal chemists notably for their promising and tunable optical properties.[1-8] The habits of these two-dimensional and well-facetted nanostructures is directly related to the very different kinetics of growth of their crystalline planes. Due to the cubic symmetry of metals, the growth of gold or silver nanoplates is obviously governed by extrinsic parameters. Although the formation of anisotropic nanostructures has been keenly discussed for decades, the respective weight of the possible driving forces involved in the growth of planar nanoparticles (NPs) is still matter of debate.[9-12] The preferential adsorption of capping agents on specific crystal facets is frequently put forward to explain anisotropic crystal growth.[13, 14] This face-blocking model is often confronted with the effects of planar defects commonly formed in face-centered-cubic (fcc) metals. Intensively studied to understand the lateral growth of macroscopic tabular crystals,[15-18] the presence of stacking faults is known to influence the structure of the nanocrystal side-faces leading to an energetically favorable 2D growth.[12] Besides these thermodynamic considerations, the supply rate of metal precursors also plays a crucial role in nanocrystal faceting that is too often overlooked.[11, 19-21] The complexity of 2D growth mechanisms requires studying at the relevant time and spatial scales the very dynamic nature of crystal growth. *In situ* Transmission Electron Microscopy (TEM) has emerged as an important step forward to follow dynamic processes in liquid environments.[22] The recent advances in the micro-fabrication of liquid cells allow investigating complex phenomena that arise at the liquid-solid interface such as the nucleation and growth of nanocrystals,[23] NPs interaction,[24, 25] electrochemical reaction,[22, 26] biological processes…[27, 28] Most studies on NP synthesis by liquid-cell TEM use the electron

beam to radiolyze the water, creating free radicals and solvated electrons that reduce metal precursors and induce nucleation and crystal growth. This radiochemical effect of the incoming electrons allows controlling the growth kinetics and consequently the morphology of nanocrystals with the electron dose. When high electron doses are used diffusion limited growth is dominant and spherical or dendritic nanostructures are formed.[29] Interestingly, Woehl and coworkers have demonstrated that under low-dose conditions the growth is then limited by the rate of the surface-reduction reaction leading to the formation of well-facetted Ag NPs.[30]

Here, we have exploited liquid TEM together with *ex situ* three-dimensional and high resolution analyses to study the growth of Au nanoplates and unravel the mechanisms determining their formation and shape. In good agreement with the silver halide model,[12, 15] our *in situ* observations provide new insights into the role of growth kinetic and crystal twinning in planar crystal habits.

Deeply investigated during the early developments of the nuclear industry, the radiolysis of water due to ionizing radiations results in the creation of well-established primary products : hydrated electrons (e_h^-), hydrogen radicals ($H^\cdot$), hydroxyl radicals ($OH^\cdot$), dihydrogen (H_2), hydrogen peroxide (H_2O_2), hydronium ions (H_3O^+), hydroperoxyl radicals ($HO_2^\cdot$). Uniformly distributed within the irradiated area, strong reducing agents (e_h^-, $H^\cdot$), being able to reduce metal ions to metallic monomers coexist with strong oxidative species ($OH^\cdot$) which can etch metallic nanostructures.[31] As the concentrations of radiation products are dose-dependent, relevant interpretation of the complex phenomena observed by liquid-cell microscopy requires a fine control over the electron irradiation. In the following, the growth of Au NPs in a 10^{-3} M $HAuCl_4$ aqueous solution was simultaneously generated and imaged with a scanning electron beam (Fig. 1b and S1). STEM HAADF imaging was performed by using the smallest probe size and

condenser aperture in order to minimize and maintain constant the beam current (i_e = 1.24 10^8 electron/s or 19.8 pA) focalized on the liquid-cell. Electron microscopists calculate the dose rate ($\dot{d}$) in electrons/Å^{2}s by dividing the beam current by the surface irradiated by the beam, which in STEM mode advantageously corresponds to the imaged area. Therefore, $\dot{d}$ was easily controlled since it is inversely proportional to the square of the magnification. With such optical conditions, $\dot{d}$ varies from 0.055 to 1.380 electrons/Å^{2}s, with a magnification ranging from 50k to 250k. The conversion of $\dot{d}$ in Gy.s^{-1} (*i.e.* J.kg^{-1}.s^{-1}), units commonly used in the field of radiation chemistry, simply requires multiplying $\dot{d}$ in electron/m^{2}s by the density normalized stopping power of water (2.798 10^5 eV.m^2/kg per electron, at 200kV)[32] and by 1.6 10^{-19} to convert electron-volts to joules. This leads to $\dot{d}$ in between 2.5 10^5 and 6.2 10^6 Gy/s for magnification ranging from 50k to 250k. This conversion allows realizing the drastic effects of beam confinement on ionizing radiations: while this dose-rate range is considered as low-dose conditions in electron microscopy, it is actually extremely high as compared to usual irradiation conditions used for the synthesis of metallic NPs by radiolytic methods.[33, 34]

The time series of images observed in figure 1a reveals the growth of well facetted Au NPs when 1mM $HAuCl_4$ solution is irradiated with $\dot{d}$ equal to 10^6 Gy/s. As the signal to noise ratio (SNR) of STEM-HAADF imaging is proportional to the thickness of mono-element nano-objects, two types of NPs can easily be distinguished after 240 seconds of growth: (i) very intense 3D NPs with smaller in-plane sizes and pentagonal or hexagonal shapes (see NP labeled d in Fig. 1a), (ii) less intense planar NPs with larger in-plane sizes and triangular or hexagonal shapes (see NP labeled c in Fig 1a). The SNR evolution of these NPs over time allows identifying both isotropic and anisotropic growth mechanisms. Indeed, while the thickness and the in-plane size of 3D NPs are continuously increasing over the experiment (Fig. 1d), the thickness of planar NPs reaches a

maximum after 80 to100 s and subsequent growth only occurs along the substrate plane (Fig. 1c).

Ex-situ three-dimensional analyses realized after unsealing the liquid-cell have confirmed the two distinct types of Au NPs synthesized on the Si_3N_4 membrane during the liquid-cell STEM experiments. High-resolution SEM unambiguously shows the presence of triangular nanoplates (i.e. nanoprisms) and hexagonal nanoplates together with 3D facetted NPs (Fig. 2a). Electron tomography combined with contrast analyses of STEM HAADF images was exploited to quantitatively analyze the shape of 3D and planar NPs. As observed in the insert of figure 2a, the distribution of SNR of nanoplates measured on 40 STEM-HAADF images follows a Gaussian distribution centered on 6.3 with a standard deviation of 1.9. Consequently, the thickness polydispersity of the nanoplates is around 30% and the thickness ratio between the thickest and the thinnest planar NPs is equal to 2.5. Electron tomography experiments were realized on nanoplates with very different STEM HAADF intensities (Fig. S2a) in order to establish the link between SNR and thickness. The precision of these nanoscale 3D analyses greatly benefits from the DART reconstruction method[35] which minimizes the artefacts due to the missing wedge (see experimental details). The thickness of a nanoplate with a low SNR (SNR = 4.9) is measured to be 16 nm (Fig 2b), whereas a nanoplate with a high SNR (SNR = 9.0) have a thickness of 29 nm (Fig S2c). Therefore, combining statistical analyses of SNR on STEM-HAADF images with quantitative measurements on an electron tomogram allowed determining an average thickness for the nanoplates of 21 ± 6.3 nm. It is worth noticing that no significant difference between the thicknesses of hexagonal and triangular nanoplates was found. Interestingly, if the restricted thickness of the nanoplates gives rise to anisotropic nanostructures with an aspect ratio up to 7, there is no straightforward relation between their thickness and in-plane size: the larger

nanoplates are not necessarily the thicker ones (Fig. 2b and S2c). By contrast, the 3D NPs are well facetted polyhedrons with a larger truncated face in contact with the substrate, but their aspect ratio is much more monodisperse and close to 1 (Fig 2c).

As the growth kinetic is an essential parameter in the formation of planar NPs, we have evidenced the effect of $\dot{d}$ on the size evolution of triangular and hexagonal nanoplates. The classical growth models usually consider the evolution of the radius of spherical NPs.[36, 37] Here, the size of planar nanostructures was defined as the diameter of their circumscribed circle (D). Figure 1e shows that the growth of both planar triangles and planar hexagons significantly accelerates when increasing the magnification and consequently $\dot{d}$. Linear regressions can reasonably be applied to the size evolution of nanoplates as a function of time (t), from which the slope corresponds to their growth rate (G_d) for each magnification. For example, the triangular NPs measured in figure 1e, have a growth rate of 0.35 nm/s, 1.59 nm/s and 3.09 nm/s for a magnification of 50k ($\dot{d}$ = 2.5 10^5 Gy/s), 100k ($\dot{d}$ = 10^6 Gy/s) and 200k ($\dot{d}$ = 4 10^6 Gy/s), respectively. The surface of planar nanostructures is given by C_1*D^2 with a geometrical factor C_1 equal to 0.325 and 0.650 for triangles and hexagons, respectively. As gold has an atomic density (d_{at}) equal to 58.9 atom/nm^3 and knowing that the thickness of the nanoplates (T) becomes rapidly constant, we can deduce the reaction rate (K) corresponding to the number of atom nucleated on a nanoplate per second by:

$$K = 2C_1 \times T \times d_{at} \times G_d^2 \times t$$

This equation reflects an antenna effect in nanocrystal growth since the reaction rate increase over time because NPs offer more adhesion sites for monomers while growing up. It is then relevant to normalize K by the surface of the NPs. However, as nanoplates have a 2D growth

mode, adhesion sites are only localized on the side faces. Therefore, the reaction rate per unit area (K_n) is given by:

$$K_n = C_2 \times G_d$$

with C_2 equal to 14.7 and 25.5 for triangles and hexagons, respectively. Interestingly, K_n depends neither on time nor on thickness, making it a relevant parameter to quantify the effects of $\dot{d}$ on nanoplate growth at the atomic scale. Dose-rate-dependent measurements of K_n were realized on a significant number of nanoplates to take into account the dispersion of NP sizes at each magnification. As seen in Figure 1f, for $\dot{d}$ ranging from 2.5 10^5 Gy/s to 4 10^6 Gy/s, K_n varies from 8.4 ± 0.9 to 51.5 ± 1.2 atoms/s.nm^2 for hexagonal platelets. Remarkably, the dose-rate dependence of K_n can be approximated with a power law $K_n \sim \dot{d}^{\alpha}$ with exponent α equal to 0.63 and 0.69 for triangular and hexagonal nanoplates, respectively. Schneider *et al.* demonstrated that the steady state concentration of radiolysis products (C_{ss}) reached after a few milliseconds of irradiation also varied as power laws of the dose rate : $C_{ss} \sim \dot{d}^{\beta}$ with β equal to 0.51 and 0.38 for e_h^- and $H^{\cdot}$, respectively.[31] Although these calculations of the composition of water subjected to the very high $\dot{d}$ of electron microscopes did not consider scanning-irradiation mode, the increase of K_n with $\dot{d}$ follows the same tendency as the concentration of reducing agents in the irradiated area, which drives the concentration of gold monomers. This behavior of K_n is consistent with a mono-molecular surface reaction with the reaction step as limiting factor. The reaction rate is then governed by a Langmuir isotherm which at low reactant concentration depends on the concentrations of adhesion sites and reactants and the rate constants for the adsorption, desorption and reaction.[38]

The growth of gold NPs is a many step process starting from the reduction of trivalent gold ions into the successive valencies up to zero-valence state, the diffusion of gold monomers towards the NPs and their reaction with the surfaces. Although it increases statistical uncertainties, we can estimate the volume of nanoplates by considering their thickness equal to 21 nm ± 6.3 nm. Indeed, as *in situ* observations revealed that the thickness of the nanoplates rapidly reaches an asymptotic value (Fig. 1c), we can reasonably extrapolate the size evolution of the nanoplates measured on projected images to the expansion of their volume, except at the early stage of the growth when planar nanostructures are also growing along the direction perpendicular to the substrate. We can then calculate the radius of an equivalent sphere (R_{eq}) in order to compare the growth of the planar and 3D NPs with the Lifshitz-Slyozov-Wagner (LSW) growth model.[36] For nanoplates with growth rate close to the average, R_{eq} varies with time as $t^{0.5}$, $t^{0.7}$ and t^{1} for a magnification of 50k, 100k and 200k, respectively (Fig. S3a). At any $\dot{d}$, we also observe that the radius (R) of 3D NPs follows the same time dependency as R_{eq} (Fig S3 b-d), revealing that planar and 3D NPs have the same dose-rate dependent volume growth. According to the LSW theory, the evolution of R (or R_{eq}) with time at low magnification (50 k) suggests again that the growth of planar and 3D NPs is limited by the surface reaction. This is also consistent with the formation of well facetted NPs which requires enough time for ad-atoms to join the energetically favorable sites.

Interestingly, the formation of nanoplates was no more observed beyond magnification of 200k and 3D NPs with branched morphologies were then synthetized (Fig S4a-b). This transition in the growth mechanisms of Au NPs is consistent with the kinetically controlled syntheses used to selectively form planar nanostructures, which consist in slowing down reduction rate. [19, 21] By considering the driving forces available for the formation of the nanostructures, Viswanath et al.

have demonstrated that low driving forces favor a layer-by-layer growth and the formation of nanoplates, whereas high driving forces lead to a continuous growth of extended 3D nanoporous structures.[20] Remarkably, our *in situ* investigations reveal that for Au NPs synthesized by radiolysis in water at room temperature, the transition between these two regimes occurs for a reaction rate per unit area around 50 atoms / s.nm^2. As the atomic densities of the most stable planes in gold, namely (111) and (100) are 13.87 and 12.01 atoms/nm^2, respectively, this reaction rate roughly corresponds to three layers per second. Besides, for magnifications over 400k ($\dot{d}$ = 1.6 10^7 Gy/s), the branched shapes tends towards dendritic structures (Fig S4c-d). As previously described, this indicates a growth limited by the diffusion of monomers, since the concentration of precursors in the local environment is severely reduced by the fast initial growth of the particles.[29, 39]

Studying dose-rate effects by liquid TEM offer unprecedented opportunities to quantify kinetic effects on the growth mechanisms of nanomaterials. However, as planar and 3D NPs grow with the same kinetic at low $\dot{d}$, the shape of the NPs is obviously also driven by thermodynamics. As the growth solution does not contain capping agents, face-blocking effects can be ruled out and the growth processes are then directly related to the atomic structure of NPs. *Ex situ* high-resolution TEM shows that both planar and 3D NPs present many stacking faults, but they differ by the orientation of their twin planes. On the one hand, 3D nanostructures have either icosahedral (Fig 3a) or decahedral shapes (Fig. 3b) with multiple-twins directly observed on HRTEM images because they are perpendicular to the substrate.[40, 41] We have determined that these 3D nanostructures are formed in majority (86 % of the NPs, statistical analysis over 1000 particles, see table S1). On the other hand, the theoretically forbidden 1/3 422 reflections observed on the Fourier transform of the HRTEM images of anisotropic nanostructures are

characteristics of twin planes oriented parallel to the substrate plane.[2] Figures 3c-e show that nanoplates are either hexagons, truncated triangles or triangles and we have measured respective probabilities of 65%, 25% and 10%. However, irrespective of their shape, all the nanoplates exhibit very large (111) faces parallel to the substrate and their sides are perpendicular to [422] directions. We have also identified the very small clusters in the vicinity of larger nanostructures to be mainly default-free truncated octahedron (Fig. 3f). In a general manner, fcc NPs tend to minimize their free energy by developing facets with the lowest surface energies corresponding to the densest atomic planes. Therefore, all the Au nanostructures formed within the liquid cell have common habits for fcc nanocrystal, which respect this basic principle of crystal faceting, since they exhibit large (111) and smaller (200) facets.[9, 40, 41] However, if the equilibrium shape of small Au clusters corresponds to the Wulff polyhedron, the morphology of larger particles is here directly related to the configuration of structural defaults. To summarize, as the growth is favor along twin planes, (111) twin planes parallel to each other lead to the formation of nanoplates, whereas other multi-twin configurations favor the growth of 3D NPs.

The conclusion above is consistent with many studies on the growth of macroscopic photographic films which shed light on the crucial role of twin planes and related side-face structures on the faceting processes in fcc planar crystals.[15-18] Based on this silver halide model, Lofton and Sigmund[12] proposed that the formation of either triangular or hexagonal nanoplates is directly related to the number of twin planes parallel to the top and bottom (111) faces. Due to the six-fold symmetry of fcc crystals along the [111] direction, a single (111) twin plane formed at an early stage of the growth results in the formation of hexagonal nuclei with alternating concave and convex side face structure (Fig 4b). As the chemical potential of surfaces is inversely proportional to their curvature,[9] concave side faces are much more attractive than

convex surfaces for gold monomers. Due to these different growth kinetics, the three concave side-faces rapidly disappear and the hexagonal nuclei transform into triangular nanoprisms with a size limited by the size of the nuclei at the time of the twinning. On the contrary, if several parallel (111) twin planes are formed at the early stage of the growth, the six sides of the hexagonal nuclei can present similar structures made of reentrant and external groves leading to the growth of planar hexagons.

As illustrated in Figure 4a, we have currently observed a shape transition of the nanoplates from triangle to hexagon when planar NPs reach a lateral size around 35 nm. Interestingly, we never observed the opposite transition. According to Lofton and Sigmund,[12] this irreversible shape transition could origin from the formation of additional twin planes in a growing single-twin nanoprism, which would equilibrate the growth kinetics of alternating side facets (Fig. 4b). We can also assume that when the growing nanoprisms reach their size limit, they subsequently growth towards hexagons because of restructuration processes of their side face structure, which are inherent to the out of equilibrium conditions of NP growth.[42-44] From geometric considerations, we can then deduce that the first twin plane which drives 2D growth, generates hexagonal nuclei with side lengths around 17 nm. This first symmetry breaking event and the formation of the subsequent stacking faults, which is not energetically costly in gold or silver, are obviously essential mechanisms of the nanoplate growth. The *in situ* analysis of these atomic-scale processes requires increasing both the frame rate of STEM imaging and magnification, resulting in a lower signal to noise ratio and much faster growth processes. Therefore, crystal defect dynamic in growing nanoparticles remains outside the scope of the reported experimental conditions, but this challenge could greatly benefit from imaging techniques that allows probing simultaneously direct and reciprocal spaces.[45]

It is worth noticing that we also observed the growth of large nanoprisms maintaining their triangular symmetry well over 35 nm in size (Fig S5a). Detailed HRTEM analyses of these rare large nanoprisms (only 1.4 % of the NPs) reveals that they exhibit rounded shape corners with no faceting perpendicular to the [422] directions (Fig S5b) and the 1/3 422 reflections on the Fourier transform of their HRTEM images (Fig. 3c and S5b) suggest the presence of several twin planes along their anisotropy axis.[2] Nevertheless, as the facets of the corners are obviously growing out of existence, their side-face structure must be more favorable for the adhesion of monomers than the side-face structure on the side of the nanoprisms. Such a phenomenon is also possible in multi-twins planar nanocrystals. For example, side-face structures made of adjacent (111) / (100) / (111) facets have a much faster growth than side-face structures composed of only (111) facets, because the sub-steps arising at the interfaces between (111) and (100) facets are preferential sites for nucleation.[16]

In conclusion, we have investigated the effects of the electron dose on the growth and faceting of planar and 3D gold NPs by *in situ* liquid STEM. We have demonstrated that our *in situ* observations allow measuring the dose-dependent growth rate of the nanoplates from which we can deduce the surface-reaction rate per unit area. This crucial parameter in chemistry kinetics has the same dose-dependent behavior than the concentration of the reducing agent in the liquid cell. More importantly, reducing the reaction rate below three atomic layers per second is a primary condition to enable the formation of nanoplates and well-facetted 3D NPs. This first experimental measurement of a critical supply rate of metal precursors for NPs faceting provides quantitative insights on the transition between growths driven by thermodynamic or kinetic effects. By exploiting *ex situ* three-dimensional analyses, we could show that the volumes of planar and 3D NPs grow with the same dose-dependent velocity. Besides, when kinetic effects

are minimized at low dose, we have also shown that the formation of either nanoplates or 3D NPs relies on twinning processes during the growth. As monomer adhesion is favored along twin planes, 2D growth requires (111) twin planes parallel to each other and the shape of the nanoplates is then directly related to the structure of their side-faces. More generally, our work demonstrates that liquid TEM is a method of choice to unravel the kinetic and thermodynamic effects on dynamical processes studied at the nanoscale, opening up avenues for understanding the growth of the rich variety of nanocrystal forms obtained by wet chemical syntheses.

Supporting Information. Experimental details, video file of NPs growth at 100k and additional data. This material is available free of charge via the Internet at http://pubs.acs.org.

Corresponding Author
* Telephone : +33 1 57 27 69 83; e-mail: damien.alloyeau@univ-paris-diderot.fr

ACKNOWLEDGMENT

The authors declare no competing financial interest.

We gratefully acknowledge the financial support of the Region Ile-de-France (convention SESAME E1845 for the JEOL ARM 200F electron microscope installed at the Paris Diderot University), the Labex SEAM (Plas-Mag project) and the CNRS (Defi-Nano Program).

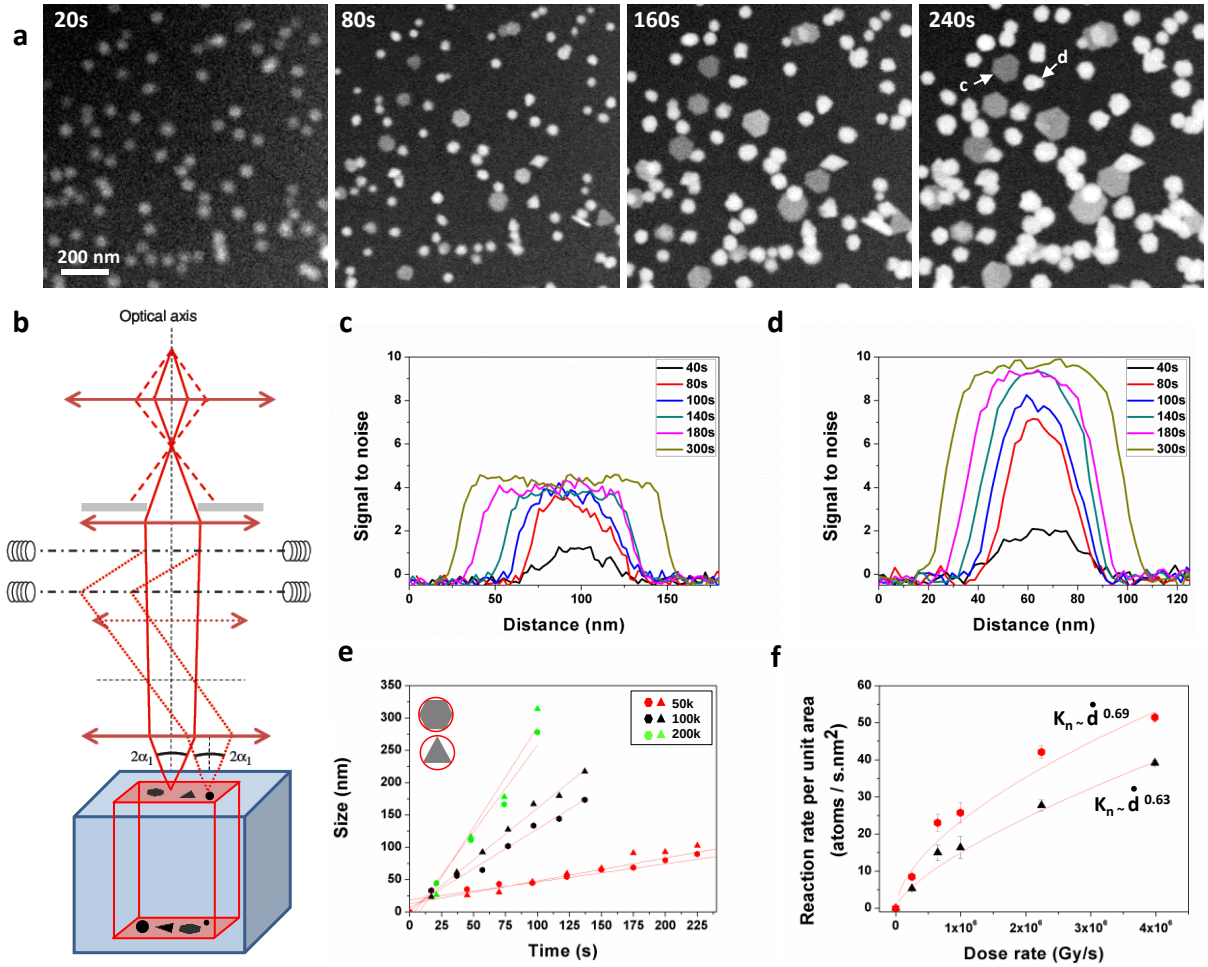

Figure 1. *In situ* follow-up of the growth of gold NPs under low-dose irradiation. (a) 1024*1024 STEM images acquired with a magnification of 100k. The dose rate was 10^6 Gy/s (0.22 electrons/A^{2}s). The irradiation time on the analyzed area is indicated in the top left corner of each image. (b) Schematic of the liquid-STEM experiment. (c) and (d) Evolution of the signal to noise ratio over time of a nanoplate (labeled c in fig. 1a) and a 3D facetted NPs (labeled d in fig. 1a), respectively. (e) Size of nanoplates as a function of time for different magnifications, 50k (red, corresponding $\dot{d}$ = 2.5 10^5 Gy/s), 100k (black, corresponding $\dot{d}$ = 10^6 Gy/s) and 200k (green, corresponding $\dot{d}$ = 4 10^6 Gy/s). The sizes of both planar nanotriangles (triangles) and planar nanohexagons (hexagons) correspond to the diameter of their circumscribed circle as indicated in the left insert. The red curves are the linear fits of the experimental data from which we can extract a growth rate (nm/s). (f) Reaction rate per unit area (K_n) for planar nanoprisms (triangles) and planar nanohexagons (hexagons) as a function of $\dot{d}$ in Gy/s. For each $\dot{d}$, mean K_n and dispersion was measured on more than 12 NPs. The red curves are the power law fits ($K_n \sim \dot{d}^{\alpha}$) of the experimental data.

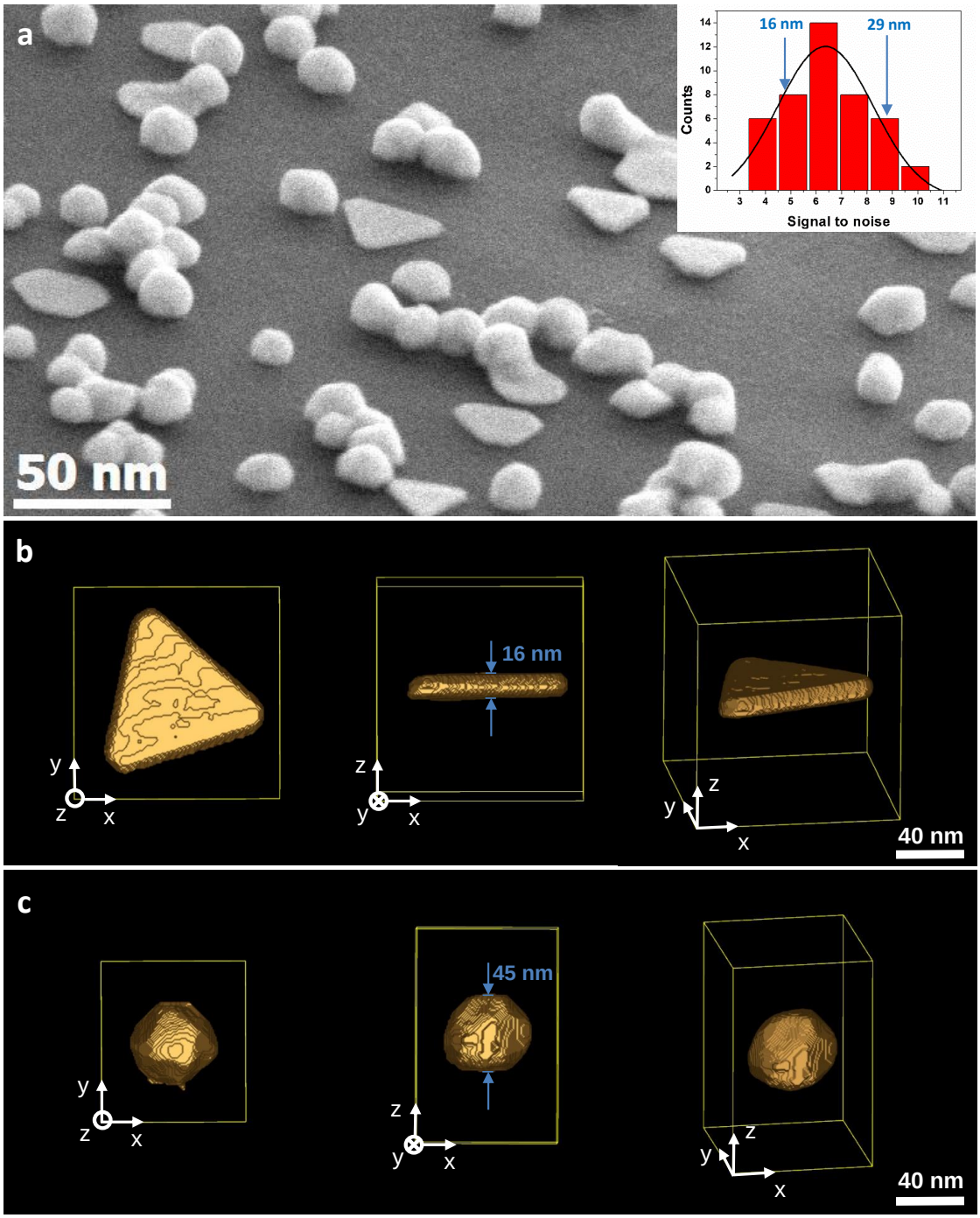

Figure 2. *Ex situ* three-dimensional analyses of the gold NPs synthesized on the Si_3N_4 membrane during the liquid-cell STEM experiments. (a) High-resolution SEM image acquired with a tilt angle of 65° confirming the formation of 3D facetted NPs and very high aspect ratio platelets (nanoprisms and nano-hexagons). In insert: distribution of signal to noise ratio of nanoplates measured on 40 STEM-HAADF images. 3D DART reconstruction calculated from electron tomography experiments. From left to right: Top view, side view and 3D view of (b) a 100 nm side nanoprism with a thickness of 16 nm and of (c) a 3D facetted NP with lateral size and thickness of 49 nm and 45 nm respectively.

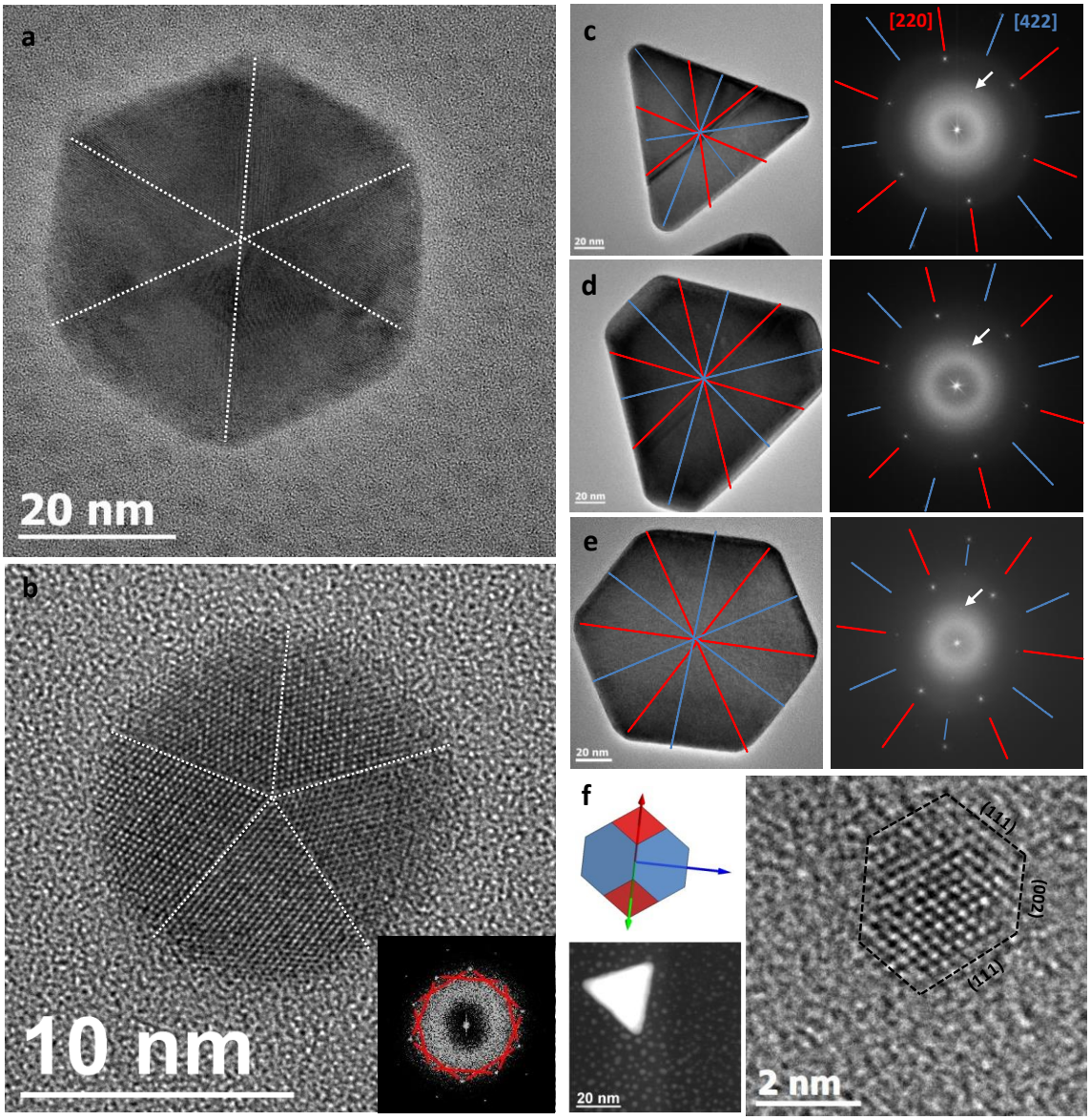

Figure 3. *Ex-situ* HRTEM analyses of the gold NPs synthesized on the Si_3N_4 membrane during the liquid-cell STEM experiments. HRTEM image of 3D NPs: (a) icosahedral NP, (b) decahedral NP (the five-fold symmetry of the [200] reflections is highlighted on the FFT in insert). Twin planes are highlighted by dashed lines. HRTEM image and corresponding FFT of planar NPs in [111] zone axis orientation: (c) nanoprism, (d) truncated nanoprism, (e) planar hexagon. The [220] and [422] crystallographic directions are indicated by red and blue lines, respectively. The white arrows indicate the theoretically forbidden 1/3 422 reflection. (f) Atomic structure of a 2 nm cluster observed in the vicinity of planar NPs (bottom left insert). The HRTEM image corresponds to a truncated octahedron with large {111} and small {200} facets observed along the [110] direction (see model in the top left insert).

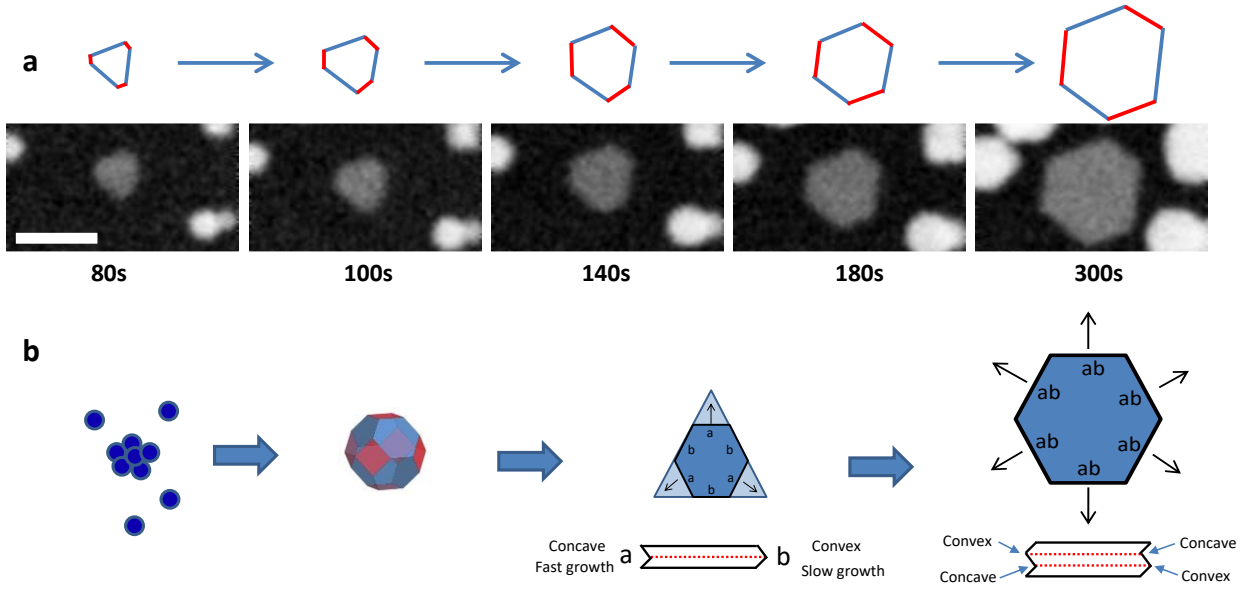

Figure 4: (a) *In situ* follow-up of the growth of a planar nanohexagon revealing a transition from a triangular to a hexagonal shape. The irradiation time on the analyzed area is indicated below each image and the scale bar corresponds to 100 nm (magnification 100 k). (b) Schematic of the proposed growth mechanisms of gold nanoplates. From left to right: the nuclei rapidly form thermodynamically stable truncated octahedrons. Then, a first twin plane (red dashed line) parallel to the top and bottom [111] faces induces the formation of triangular prisms due to their alternating side structures with concave (fastly growing a-type faces) and convex (slowly growing b-type faces) orientations.[12] When additional twin planes appear all the sides start growing homogenously leading to the formation of hexagonal nanostructures, because they all contain concave and convex orientations.

Table of Contents Graphic

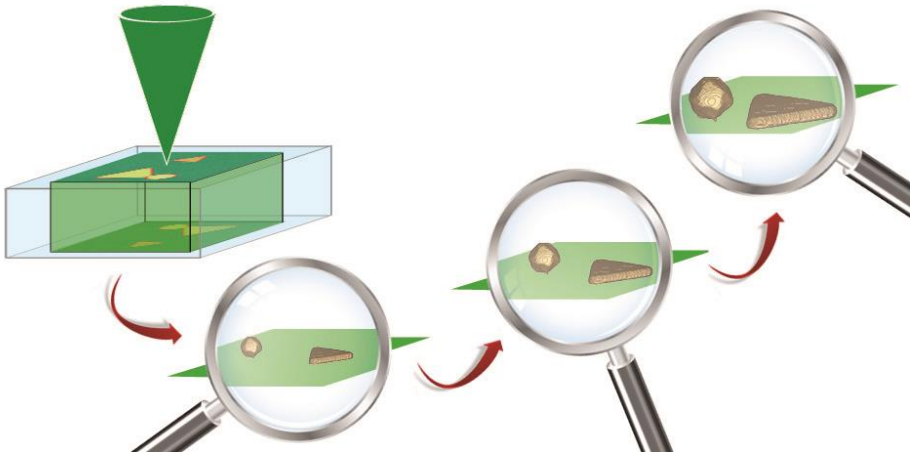

Synopsis

We have exploited *in situ* liquid TEM together with *ex situ* three-dimensional and high-resolution analyses to understand the growth of gold nanoplates. By measuring the dose-dependent expansion of the nanoparticle volume, we have determined a critical supply rate of gold monomers for the anisotropic growth and faceting of gold nanoparticles: the formation of facetted planar nanostructures requires maintaining the growth rate below three atomic layers per seconds. Besides this quantitative insights on the transition between growths driven by thermodynamic or kinetic effects, we have also shown that the formation of either nanoplates or 3D NPs relies on twinning processes during the growth.

REFERENCES

1. Beischer, D.; Krause, F. *Naturwissenschaften* **1937,** 25, 825-829.
2. Kirkland, A. I.; Jefferson, D. A.; Duff, D. G.; Edwards, P. P.; Gameson, I.; Johnson, B. F. G.; Smith, D. J. *Proc. R. Soc. London Ser. A-Math. Phys. Eng. Sci.* **1993,** 440, 589-609.
3. Jin, R. C.; Cao, Y. W.; Mirkin, C. A.; Kelly, K. L.; Schatz, G. C.; Zheng, J. G. *Science* **2001,** 294, 1901-1903.
4. Wang, C. S.; Kan, C. X.; Zhu, J. J.; Zeng, X. L.; Wang, X. F.; Li, H. C.; Shi, D. N. *J. Nanomater.* **2010**, 9.
5. Chu, H.-C.; Kuo, C.-H.; Huang, M. H. *Inorganic Chemistry* **2005,** 45, 808-813.
6. Shao, Y.; Jin, Y. D.; Dong, S. J. *Chem. Commun.* **2004**, 1104-1105.
7. Sun, X. P.; Dong, S. J.; Wang, E. K. *Langmuir* **2005,** 21, 4710-4712.
8. Sau, T. K.; Murphy, C. J. *J. Am. Chem. Soc.* **2004,** 126, 8648-8649.
9. Xia, Y. N.; Xiong, Y. J.; Lim, B.; Skrabalak, S. E. *Angew. Chem.-Int. Edit.* **2009,** 48, 60-103.
10. Grzelczak, M.; Perez-Juste, J.; Mulvaney, P.; Liz-Marzan, L. M. *Chem. Soc. Rev.* **2008,** 37, 1783-1791.
11. Millstone, J. E.; Hurst, S. J.; Métraux, G. S.; Cutler, J. I.; Mirkin, C. A. *Small* **2009,** 5, 646-664.
12. Lofton, C.; Sigmund, W. *Adv. Funct. Mater.* **2005,** 15, 1197-1208.
13. Sun, Y.; Mayers, B.; Herricks, T.; Xia, Y. *Nano Lett.* **2003,** 3, 955-960.
14. Zeng, J.; Xia, X.; Rycenga, M.; Henneghan, P.; Li, Q.; Xia, Y. *Angew. Chem., Int. Ed.* **2011,** 50, 244-249.
15. Berriman, R. W.; Herz, R. H. *Nature* **1957,** 180, 293-294.
16. Bogels, G.; Meekes, H.; Bennema, P.; Bollen, D. *J. Cryst. Growth* **1998,** 191, 446-454.
17. Bogels, G.; Pot, T. M.; Meekes, H.; Bennema, P.; Bollen, D. *Acta Crystallogr. Sect. A* **1997,** 53, 84-94.
18. Goessens, C.; Schryvers, D.; Vanlanduyt, J.; Amelinckx, S.; Verbeeck, A.; Dekeyzer, R. *J. Cryst. Growth* **1991,** 110, 930-941.
19. Le Beulze, A.; Duguet, E.; Mornet, S.; Majimel, J.; Treguer-Delapierre, M.; Ravaine, S.; Florea, I.; Ersen, O. *Langmuir* **2014,** 30, 1424-1434.
20. Viswanath, B.; Kundu, P.; Halder, A.; Ravishankar, N. *J. Phys Chem. C* **2009,** 113, 16866-16883.

21. Xiong, Y.; McLellan, J. M.; Chen, J.; Yin, Y.; Li, Z.-Y.; Xia, Y. *J. Am. Chem. Soc.* **2005,** 127, 17118-17127.
22. Williamson, M. J.; Tromp, R. M.; Vereecken, P. M.; Hull, R.; Ross, F. M. *Nat. Mater.* **2003,** 2, 532-536.
23. Liao, H. G.; Niu, K. Y.; Zheng, H. M. *Chem. Commun.* **2013,** 49, 11720-11727.
24. Liu, Y. Z.; Lin, X. M.; Sun, Y. G.; Rajh, T. *J. Am. Chem. Soc.* **2013,** 135, 3764-3767.
25. Park, J.; Zheng, H. M.; Lee, W. C.; Geissler, P. L.; Rabani, E.; Alivisatos, A. P. *Acs Nano* **2012,** 6, 2078-2085.
26. White, E. R.; Singer, S. B.; Augustyn, V.; Hubbard, W. A.; Mecklenburg, M.; Dunn, B.; Regan, B. C. *Acs Nano* **2012,** 6, 6308-6317.
27. de Jonge, N.; Peckys, D. B.; Kremers, G. J.; Piston, D. W. *Proc. Natl. Acad. Sci. U. S. A.* **2009,** 106, 2159-2164.
28. Peckys, D. B.; de Jonge, N. *Nano Lett.* **2011,** 11, 1733-1738.
29. Kraus, T.; de Jonge, N. *Langmuir* **2013,** 29, 8427-8432.
30. Woehl, T. J.; Evans, J. E.; Arslan, I.; Ristenpart, W. D.; Browning, N. D. *Acs Nano* **2012,** 6, 8599-8610.
31. Schneider, N. M.; Norton, M. M.; Mendel, B. J.; Grogan, J. M.; Ross, F. M.; Bau, H. H. *J. Phys. Chem. C* **2014,** 118, 22373-22382.
32. M.J. Berger; J.S. Coursey; M.A. Zucker; J. Chang. *NIST Standard Reference Database 124* **1998,** http://www.nist.gov/pml/data/star/.
33. Abidi, W.; Selvakannan, P. R.; Guillet, Y.; Lampre, I.; Beaunier, P.; Pansu, B.; Palpant, B.; Remita, H. *J. Phy. Chem. C* **2010,** 114, 14794-14803.
34. Gachard, E.; Remita, H.; Khatouri, J.; Keita, B.; Nadjo, L.; Jacqueline Belloni, a. *New J. Chem.* **1998,** 22, 1257-1265.
35. Batenburg, K. J.; Bals, S.; Sijbers, J.; Kübel, C.; Midgley, P. A.; Hernandez, J. C.; Kaiser, U.; Encina, E. R.; Coronado, E. A.; Van Tendeloo, G. *Ultramicroscopy* **2009,** 109, 730-740.
36. Lifshitz, I. M.; Slyozov, V. V. *J. Phys. Chem. Solids* **1961,** 19, 35-50.
37. Viswanatha, R.; Sarma, D. D., Growth of Nanocrystals in Solution. In *Nanomaterials Chemistry*, Wiley-VCH Verlag GmbH & Co. KGaA: 2007; pp 139-170.
38. Laidler, K. J., *Chemical Kinetics*. Harper & Row: New York, 1987.
39. Witten, T.; Sander, L. *Phys. Rev. Lett.* **1981,** 47, 1400-1403.
40. Elechiguerra, J. L.; Reyes-Gasga, J.; Yacaman, M. J. *J. Mater. Chem.* **2006,** 16, 3906-3919.
41. Huang, L.; Shan, A.; Li, Z.; Chen, C.; Wang, R. *CrystEngComm* **2013,** 15, 2527-2531.
42. Andreazza, P.; Mottet, C.; Andreazza-Vignolle, C.; Penuelas, J.; Tolentino, H. C. N.; De Santis, M.; Felici, R.; Bouet, N. *Phys. Rev. B* **2010,** 82, 155453.
43. Langlois, C.; Alloyeau, D.; Le Bouar, Y.; Loiseau, A.; Oikawa, T.; Mottet, C.; Ricolleau, C. *Faraday Discuss.* **2008,** 138, 375 - 391.
44. Rellinghaus, B.; Dmitrieva, O.; Stappert, S. *J. Cryst. Growth* **2004,** 262, 612-619.
45. Alloyeau, D.; Ricolleau, C.; Oikawa, T.; Langlois, C.; Le Bouar, Y.; Loiseau, A. *Ultramicroscopy* **2008,** 108, 656-662.